Supramolecular organization of membrane proteins with anisotropic hydrophobic thickness

Journal:	*Soft Matter*
Manuscript ID	SM-ART-02-2019-000358.R1
Article Type:	Paper
Date Submitted by the Author:	26-Apr-2019
Complete List of Authors:	Kahraman, Osman; University of Southern California Haselwandter, Christoph; University of Southern California

SCHOLARONE™
Manuscripts

Journal Name

ARTICLE TYPE

Supramolecular organization of membrane proteins with anisotropic hydrophobic thickness

Osman Kahraman[a,‡] and Christoph A. Haselwandter[a]

Experiments have revealed that membrane proteins often self-assemble into locally ordered clusters. Such membrane protein lattices can play key roles in the functional organization of cell membranes. Membrane protein organization can be driven, at least in part, by bilayer-mediated elastic interactions between membrane proteins. For membrane proteins with anisotropic hydrophobic thickness, bilayer-mediated protein interactions are inherently directional. Here we establish general relations between anisotropy in membrane protein hydrophobic thickness and supramolecular membrane protein organization. We show that protein symmetry is distinctively reflected in the energy landscape of bilayer-mediated protein interactions, favoring characteristic lattice architectures of membrane protein clusters. We find that, in the presence of thermal fluctuations, anisotropy in protein hydrophobic thickness can induce membrane proteins to form mesh-like structures dividing the membrane into compartments. Our results help to elucidate the physical principles and mechanisms underlying the functional organization of cell membranes.

1 Introduction

Many essential biological functions of cell membranes rely on the organization of membrane proteins into specialized membrane regions with differentiated structure and function[1]. Notably, recent advances in high-resolution imaging techniques have shown that integral membrane proteins, such as the receptor components of various signaling networks, can self-assemble into large clusters comprising hundreds of proteins[2,3] with locally ordered lattice architectures[4–6]. Clustering can directly impact the functional characteristics of membrane proteins by, for instance, facilitating localized signal transduction[7] and increasing precision and adaptation in signal processing[8,9]. The differentiated clustering of a particular type of membrane protein can also influence how other, unclustered, membrane proteins and lipids diffuse and interact with each other[10,11]. Elucidation of the physical mechanisms and principles governing the self-assembly and architecture of membrane protein lattices is therefore of critical importance for a quantitative understanding of the supramolecular organization and associated collective functional properties of cell membranes.

Supramolecular organization of membrane proteins can be driven by direct protein-protein interactions[12–14]. Moreover, experiments[15–20] and computational modeling[21–25] suggest that lipid bilayer-mediated interactions between membrane proteins provide a general design principle for membrane organization independent of any specific protein-protein contacts. Bilayer-mediated protein interactions are typically longer-ranged than direct protein-protein interactions in the membrane. Clustering of membrane proteins via bilayer-mediated protein interactions has been studied extensively within the framework of continuum elasticity theory[15,26–50]. For membrane proteins that do not have perfect rotational symmetry in the plane of the membrane, bilayer-protein interactions tend to be anisotropic. The continuum elasticity theory of membranes implies that anisotropy in bilayer-protein interactions can strongly affect the regulation of protein function by lipid bilayer mechanics[24,25,51,52] and induce directionality in bilayer-mediated protein interactions[45,47,49,52–54]. Directional, bilayer-mediated protein interactions provide a physical mechanism for the self-assembly as well as local ordering of membrane protein lattices, and can induce cooperativity among the proteins forming membrane protein lattices[24,25,45,50,52,54,55].

Based on the structural biology of membrane proteins, one may distinguish between two, not mutually exclusive, molecular origins of anisotropy in bilayer-protein interactions and, hence, directionality in bilayer-mediated protein interactions. On the one hand, the shape of the cross section of membrane proteins in the plane of the membrane may not show continuous rotational symmetry about the protein center. The resulting directionality of bilayer-mediated protein interactions can yield, depending on the oligomeric state and shape of the membrane protein, distinctive supramolecular lattice architectures of membrane protein clusters[52,55]. On the other hand, the shape of a membrane protein may show, to a first approximation, continuous rotational symme-

[a] Department of Physics & Astronomy and Department of Biological Sciences, University of Southern California, Los Angeles, CA 90089, USA.
[‡] Present address: R & D Center, Arcelik A.S., Tuzla, Istanbul, 34950, Turkey.

try in the plane of the cell membrane, but the bilayer-protein interactions along the bilayer-protein interface may change with the azimuthal angle about the protein center (see Fig. 1). The aim of this article is to explore this latter scenario, and to establish general relations between the azimuthal symmetry of bilayer-protein interactions and the supramolecular organization of membrane proteins. We thereby focus on bilayer-mediated protein interactions due to protein-induced lipid bilayer thickness deformations, which have been found to play a central role in the supramolecular organization of a variety of membrane proteins [15–20,23].

To single out the effect of azimuthal protein symmetry on the directionality of bilayer-thickness-mediated protein interactions, we consider here cylindrical membrane protein shapes with a periodic variation in the protein hydrophobic thickness along the bilayer-protein interface (Fig. 1). On the one hand, such periodic variations in the protein hydrophobic thickness may arise in protein oligomers composed of repeating protein subunits, which is a general motif of membrane protein structure [56,57]. On the other hand, cylindrical membrane inclusions with varying hydrophobic thickness provide a mathematical representation of non-cylindrical membrane protein shapes [45,51], and can thus be used to model bilayer-protein interactions even for membrane proteins that have a constant hydrophobic thickness and a non-cylindrical shape. We show that the bilayer-thickness-mediated interactions between such "crown-shaped proteins" yield self-assembly of protein clusters with distinctive ground state lattice architectures determined by the azimuthal symmetry of bilayer-protein interactions. For the case of crown-shaped proteins with one-fold rotational symmetry, our calculations predict that thermal perturbations to the corresponding ground state lattice architectures can yield mesh-like supramolecular protein assemblies with typical mesh sizes > 20 nm, thus producing membrane compartmentalization at scales that exceed the typical size of individual proteins [1,58,59]. Taken together, our results provide general links between anisotropy in bilayer-protein interactions and supramolecular membrane protein organization, and suggest simple physical mechanisms underlying the structural and functional organization of cell membranes.

2 Modeling anisotropic bilayer-protein interactions

Lipid bilayer-mediated interactions between membrane proteins may arise [15,26–50,52–55,60,61] from protein-induced lipid bilayer curvature or thickness deformations, as well as bilayer fluctuations. We focus here on protein-induced lipid bilayer thickness deformations, which have been found to induce protein clustering in experiments on a broad range of membrane proteins [15–20,23], and which provide a general mechanism for the regulation of protein function by bilayer mechanics [39,62,63]. In the simplest model, the energy cost of protein-induced lipid bilayer thickness deformations is given by the continuum elastic energy [62–64]

$$G = \frac{1}{2} \int \mathrm{d}x \mathrm{d}y \left[K_b (\nabla^2 u)^2 + K_t \left(\frac{u}{a} \right)^2 \right], \quad (1)$$
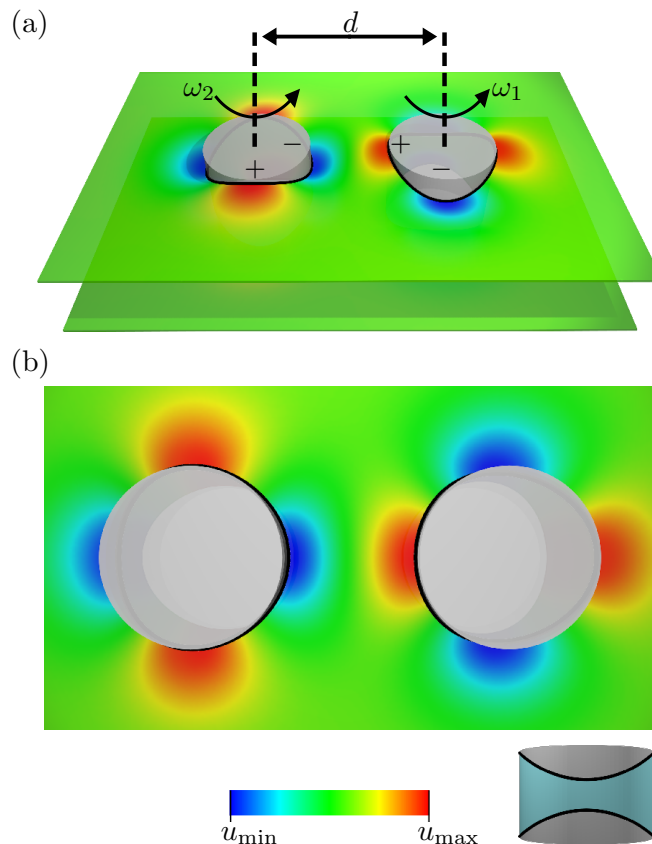
Fig. 1 (a) Side and (b) top-down views of the lipid bilayer thickness deformations induced by membrane proteins with anisotropic hydrophobic thickness. The protein-induced lipid bilayer thickness deformations u were calculated by minimizing eqn (1) using finite elements (FEs) [47,49,55], and depend on key molecular properties of the lipids and proteins (see Sec. 2), the protein center-to-center distance d, and the protein orientations $\omega_{1,2}$. We single out the effect of anisotropy in protein hydrophobic thickness on the directionality of bilayer-thickness-mediated protein interactions by employing the crown model of membrane proteins in eqn (2), which is illustrated in the lower right corner of panel (b) with the surface enclosed by the two black curves representing the hydrophobic surface of the membrane protein. The protein hydrophobic thickness is also indicated by black curves in the main panels of (a) and (b), with minima and maxima in the protein hydrophobic thickness being denoted by $-$ and $+$ signs in panel (a). We set here $s = 2$, $\omega_1 = 0$, $\omega_2 = \pi/2$, and $d = 8$ nm. The same color scale in u is used for panels (a) and (b) with $u_{\min} = -0.6$ nm and $u_{\max} = 0.4$ nm.

where the thickness deformation field $u(x,y)$ is one-half the protein-induced perturbation in bilayer hydrophobic thickness, K_b is the lipid bilayer bending rigidity, K_t is the lipid bilayer thickness deformation modulus, and a is one-half the hydrophobic thickness of the unperturbed lipid bilayer. In eqn (1) we have, for simplicity, set the membrane tension equal to zero. The values of the effective parameters K_b, K_t, and a in eqn (1) depend on the molecular properties of the lipids forming the lipid bilayer, such as the lipid tail length [65]. We use here the values $K_b = 20 \, k_B T$, $K_t = 60 \, k_B T / \mathrm{nm}^2$, and $a = 1.6$ nm typical for a broad range of *in vitro* and *in vivo* systems [39,63,66]. Once the values of K_b, K_t, and a have been fixed, the model in eqn (1) has the appealing property that it does not involve any free parameters, with the (minimal)

energy cost of protein-induced lipid bilayer thickness deformations being determined solely by the boundary conditions on u at the bilayer-protein interfaces.

Following the standard elasticity theory of lipid bilayer-protein interactions[39,63], we assume that integral membrane proteins are much more rigid than lipid bilayers, and therefore model membrane proteins as rigid membrane inclusions with fixed hydrophobic thickness. As examined previously[45,47,49,52,55] and discussed above, directionality of bilayer-thickness-mediated protein interactions may originate from a non-circular cross section of membrane proteins in the plane of the membrane. We consider here the complementary scenario in which directionality of bilayer-thickness-mediated protein interactions arises solely from azimuthal variations in the protein hydrophobic thickness along the bilayer-protein interface, with a circular cross section of the membrane protein. In particular, we focus on the crown model of membrane proteins[45,49] (Fig. 1), which allows us to single out the effect of anisotropy in protein hydrophobic thickness on supramolecular membrane protein organization. In this model, each membrane protein i is modeled as a cylindrical membrane inclusion with a hydrophobic thickness U_i that varies along the bilayer-protein interface according to[45,49]

$$U_i(\theta_i) = U_i^0 + \delta_i \cos(s(\theta_i - \omega_i)), \qquad (2)$$

where θ_i is the azimuthal angle associated with a polar coordinate system with the center of membrane protein i as the origin, U_i^0 is the average hydrophobic mismatch, δ_i is the magnitude of mismatch modulations, s is the protein symmetry, and ω_i is the orientation of membrane protein i (Fig. 1). The values of U_i^0, δ_i, and s in eqn (2) generally depend on the specific type of membrane protein under consideration. For the numerical calculations described here we use $U_i^0 = -0.1$ nm and $\delta_i = 0.5$ nm[49]. Furthermore, we use a protein radius $R_i = 2.3$ nm[49], which corresponds to the approximate size of the closed pentameric state of the bacterial mechanosensitive channel of large conductance[67]. In accordance with previous work[36,62,68], we impose zero-slope boundary conditions at the bilayer-protein interface.

For membrane proteins in close enough proximity, the protein-induced lipid bilayer thickness deformations overlap, resulting in bilayer-thickness-mediated protein interactions[27,28,32,34–36,52,60]. The bilayer-thickness-mediated protein interactions implied by eqn (1) for the crown-shaped proteins in eqn (2) can be calculated using analytic[45,49,51,52] and finite element (FE)[47,49,55] methods. Both of these approaches allow the accurate minimization of eqn (1) for membrane proteins of arbitrary symmetry and shape for arbitrary protein separations and protein orientations. For the calculations described here we employed the FE scheme described in detail in Ref.[49], which is particularly suitable for systems composed of many (strongly) interacting membrane proteins. This FE scheme allows[47,49,55] the numerically reliable and efficient minimization of eqn (1) subject to the bilayer-protein boundary conditions even for membranes containing hundreds of (strongly) interacting membrane proteins with complicated bilayer-protein boundary conditions, and is therefore suitable for exploring the supramolecular organization of membrane proteins with anisotropic hydrophobic thickness.

3 Directionality of bilayer-mediated protein interactions

Before exploring the bilayer-mediated protein interactions implied by eqn (2), it is useful to consider the particularly straightforward scenario of a single membrane protein with a circular cross section in the plane of the membrane and a constant hydrophobic thickness, which corresponds to $\delta_i = 0$ in eqn (2). For such a single membrane protein, the protein-induced lipid bilayer thickness deformation field u only depends on the radial coordinate about the protein center, with the u minimizing eqn (1) being given by a sum of zeroth-order modified Bessel functions of the second kind[62,69]. As a result, one obtains[49,62,69], in the radial direction about the protein center, a series of expansion and compression zones of u, with an approximately exponential dampening of the magnitude of u.

When two cylindrical membrane proteins with constant hydrophobic thickness come into vicinity of each other, the bilayer thickness deformation fields induced by the two proteins overlap, yielding bilayer-thickness-mediated protein interactions. Depending on the separation of the two proteins, the overlap between expansion and compression zones of u may be in phase or out of phase, resulting in favorable or unfavorable interactions between membrane proteins[36,45,47,49,52], respectively. For membrane proteins with non-cylindrical shapes or with—as in the crown model in eqn (2)—azimuthal variations in the protein's hydrophobic thickness, the protein-induced lipid bilayer thickness deformations bear a characteristic signature of the protein anisotropy (Fig. 1). As a result, for such membrane proteins the sign and magnitude of bilayer-thickness-mediated protein interactions not only depend on the protein separation but also on the protein orientation.

Figure 2 shows the energy of bilayer-thickness-mediated protein interactions for a pair of crown-shaped proteins as a function of the protein orientations ω_1 and ω_2 for three different protein symmetries $s = 1$, 2, and 3 at small (strong interactions, $d = 6$ nm in Fig. 2a) and intermediate (weak interactions, $d = 10.5$ nm in Fig. 2b) protein separations. To understand how the "egg-carton" energy landscapes in Fig. 2 emerge from the anisotropic bilayer deformations induced by the two proteins, it is useful to consider three distinctive pair configurations: (i) the $+/-$ configuration, in which the bilayer-protein boundary regions with maximal and minimal hydrophobic thickness face each other (Fig. 1) and which occurs, for instance, at $\omega_1 = 0$ and $\omega_2 = 0$ for odd s and at $\omega_1 = 0$ and $\omega_2 = \pi/s$ for even s; (ii) the $-/-$ configuration, in which the bilayer-protein boundary regions with minimal hydrophobic thickness face each other and which occurs, for instance, at $\omega_1 = 0$ and $\omega_2 = \pi/s$ for odd s and at $\omega_1 = \pi/s$ and $\omega_2 = \pi/s$ for even s; (iii) the $+/+$ configuration, in which the bilayer-protein boundary regions with maximal hydrophobic thickness face each other and which occurs, for instance, at $\omega_1 = \pi/s$ and $\omega_2 = 0$ for odd s and at $\omega_1 = 0$ and $\omega_2 = 0$ for even s.

We first consider the energy landscapes in Fig. 2a obtained for small protein separations. For the $+/-$ configuration, the undu-
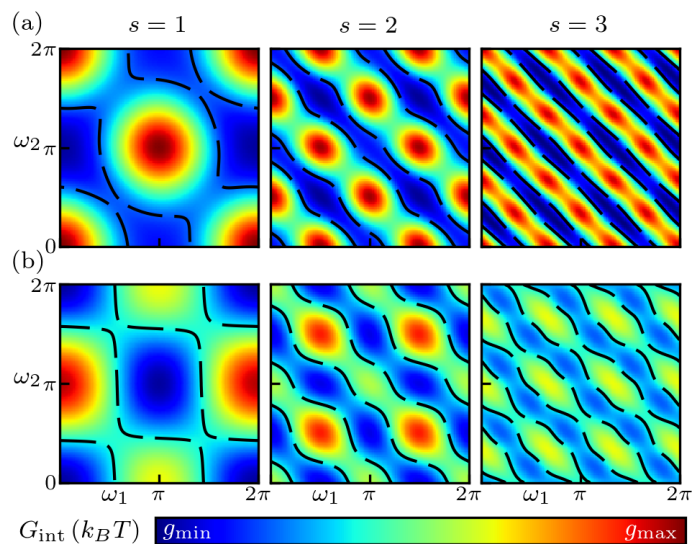
Fig. 2 Bilayer-thickness-mediated pair interaction energies G_{int} for two crown-shaped proteins with $s = 1, 2$, and 3 in eqn (2) as a function of the protein orientations ω_1 and ω_2 at the center-to-center protein separations (a) $d = 6$ nm and (b) $d = 10.5$ nm, computed by minimizing eqn (1) using FEs [47,49]. The color scale in G_{int} corresponds to $(g_{min}, g_{max}) = (-22, 76)\ k_BT$ in panel (a) and to $(g_{min}, g_{max}) = (-0.6, 1)\ k_BT$ in panel (b). The dashed lines indicate contours with $G_{int} = 0$.

lations of the thickness deformations induced by the two proteins are out of phase. This means that, due to the substantial overlap of compression and expansion zones, the bilayer thickness deformations in the membrane region separating the two proteins are strongly frustrated, yielding highly unfavorable bilayer-thickness-mediated protein interactions (Fig. 2a). In contrast, for protein configurations with protein-induced lipid bilayer thickness deformations that are in phase with each other, such as the $+/+$ and $-/-$ configurations in Fig. 2a, there is substantial overlap of compression or expansion zones, which reduces the overall deformation footprint of the two proteins and yields highly favorable bilayer-thickness-mediated protein interactions. Note that we used here an average protein hydrophobic thickness $U_i^0 < 0$, which generally results in a greater magnitude of u in compression zones than in expansion zones. As a result, the $-/-$ configuration in Fig. 2a generally yields more favorable bilayer-thickness-mediated protein interactions than the $+/+$ configuration. As the proteins are rotated about their centers at fixed d, the energy of bilayer-thickness-mediated protein interactions changes smoothly between the $+/-$, $-/-$, and $+/+$ configurations. However, the period and precise location in $\omega_{1,2}$ of the $+/-$, $-/-$, and $+/+$ configurations vary with the protein symmetry s, resulting in distinctive energy landscapes for $s = 1, 2$, and 3 in Fig. 2a.

At an intermediate protein separation $d = 10.5$ nm, we find in Fig. 2b energy landscapes of bilayer-thickness-mediated protein interactions that are qualitatively similar to those obtained in Fig. 2a at small protein separations but with much weaker interaction energies. In particular, we find energy differences of less than $2\ k_BT$ between the most favorable and most unfavorable protein configurations in Fig. 2b, but energy differences of almost $100\ k_BT$ for the corresponding protein configurations

in Fig. 2a. Furthermore, we find that favorable and unfavorable regions of the interaction energy landscapes are reversed in Fig. 2b compared to Fig. 2a. This can be understood by noting that, as discussed above, eqn (1) implies alternating expansion and compression zones of u in the radial direction about the protein center [62,69]. As a result, a decrease or increase in d can lead to a switch between overlapping expansion or compression zones of the protein-induced bilayer thickness deformations [49,52] and, hence, a shift in the "phase" of the energy landscape. Taken together, the results in Fig. 2 show that anisotropy in protein hydrophobic thickness can yield strong directionality in bilayer-thickness-mediated protein interactions, with a subtle dependence of the energy landscape of bilayer-thickness-mediated protein interactions on the protein orientation and separation as well as the protein symmetry.

4   Ground state lattice architectures

The results in Sec. 3 suggest that, similarly as in the case of membrane proteins with a non-circular cross section in the plane of the membrane [52,55], the directionality of bilayer-thickness-mediated interactions between crown-shaped proteins may affect large-scale protein organization, with different protein symmetries favoring different protein lattice architectures. Figure 3 shows the bilayer-thickness-mediated protein interaction energy per protein, G_{int}, for protein clusters composed of hundreds of crown-shaped proteins with $s = 1, 2$, and 3 in eqn (2) as a function of the center-to-center distance between neighboring proteins, d. Table 1 summarizes the energetically most favorable protein configurations implied by Fig. 3.

We consider in Fig. 3 the three regular tilings of the Euclidean plane corresponding to honeycomb, square, and hexagonal lattice architectures. As discussed below, trimers of crown-shaped proteins provide an energetically favorable nearest-neighbor interaction motif, and we therefore also allow in Fig. 3 for kagome lattices, which combine regular triangular and hexagonal tilings. All of the results in Fig. 3 were obtained from the full multi-body interaction energies calculated through minimization of eqn (1) using FEs [47,49,55]. We consider in Fig. 3 values of d such that $d \geqslant d_{st}$, where d_{st} is the smallest protein separation allowed by steric constraints on lipid size. We used here $d_{st} = 5.6$ nm so that the minimum edge-to-edge protein separation $\geqslant 1$ nm. We employed, for each s and lattice symmetry in Fig. 3, a fixed set of protein orientations ω_i. We obtained these ω_i by optimizing, through Monte Carlo simulations with simulated annealing of pair interaction potentials (see Appendix A), ω_i at $d = 6$ nm, which corresponds to the strongly-interacting regime in Fig. 2. In the absence of any constraints on the protein separation preventing $d \rightarrow d_{st}^+$, the strongly-interacting regime is expected to set the ground state lattice architecture of membrane protein lattices. If there are additional constraints on d prohibiting $d \rightarrow d_{st}^+$, protein orientations different from those studied here may be dominant from an energetic perspective.

We first consider crown-shaped proteins with $s = 1$ (see Fig. 3a). We find that all of the lattice symmetries considered in Fig. 3a yield a qualitatively similar dependence of G_{int} on d. In particular, for 8 nm $\lesssim d \lesssim 11$ nm the interaction energies are
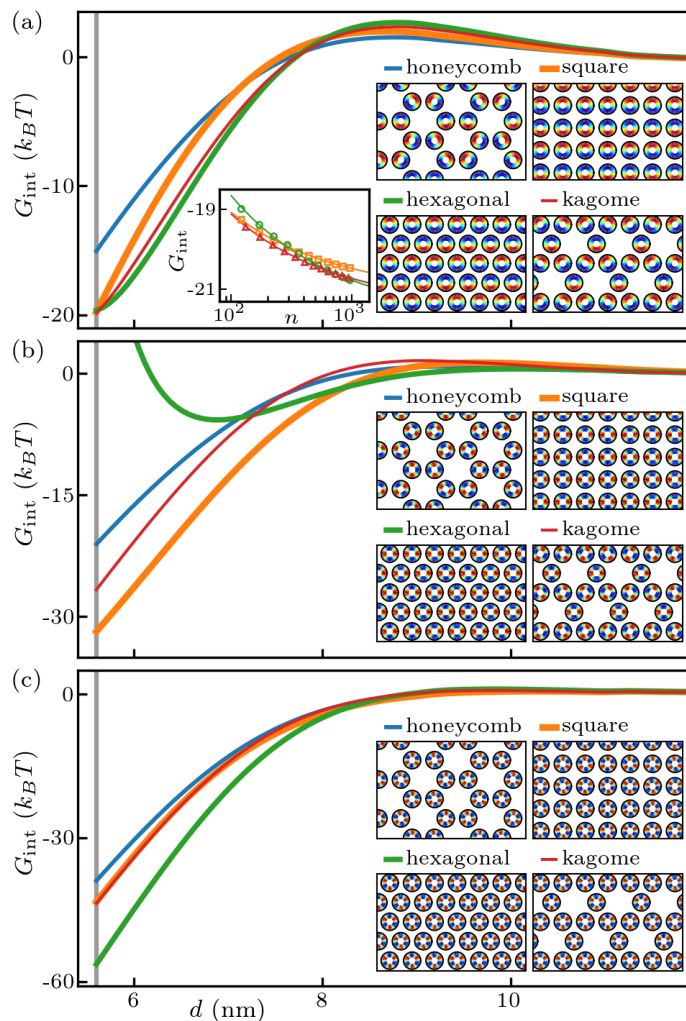
Fig. 3 Interaction energy per protein due to bilayer-thickness-mediated protein interactions, G_{int}, for honeycomb, square, hexagonal, and kagome lattices of crown-shaped proteins versus center-to-center distance between neighboring proteins, d, for (a) $s = 1$, (b) $s = 2$, and (c) $s = 3$ in eqn (2) calculated by minimizing eqn (1) using FEs [47,49,55]. We constructed the honeycomb lattices from 216 proteins, the kagome lattices from 222 proteins, and the square and hexagonal lattices from 225 proteins each. The vertical lines show $d = d_{\text{st}}$. The coloring of crown-shaped proteins in the insets follows the u-scale in Fig. 1. For each lattice symmetry, the protein orientations were fixed as indicated in the insets using Monte Carlo simulations with simulated annealing of pair interaction potentials at $d = 6$ nm (see Appendix A). The protein configurations in the insets correspond to $d = 6$ nm. The leftmost inset in panel (a) shows G_{int} in units of $k_B T$ at $d = d_{\text{st}}$ as a function of the protein number n in square (squares), hexagonal (circles), and kagome (triangles) lattices together with the fits of this data to eqn (3) (solid curves).

weakly unfavorable, and $|G_{\text{int}}| < 1\ k_B T$ for $d \gtrsim 11$ nm. In contrast, for $d \lesssim 8$ nm we find (strongly) favorable G_{int} for all the lattice symmetries considered in Fig. 3a, with the energetically most favorable states corresponding to the smallest value of d allowed by steric constraints, $d = d_{\text{st}}$. Qualitatively similar interaction potentials arise for pairs of membrane proteins with constant hydrophobic thickness and circular as well as non-circular cross sections in the plane of the membrane [36,45,47,49,52,55].

Table 1 Summary of energetically most favorable protein lattice symmetries and corresponding azimuthal ordering motifs in Fig. 3 for $s = 1$, $s = 2$, and $s = 3$ in eq. (2). For $s = 1$, we find an effectively degenerate ground state lattice architecture, with the interaction energies G_{int} associated with hexagonal, square, and kagome lattices lying within 1 $k_B T$ of each other (see main text).

Protein symmetry	Lattice symmetry	Azimuthal ordering
$s = 1$	Hexagonal (degenerate)	$+/+/+$ and $-/-/-$
$s = 1$	Square (degenerate)	$+/+$ and $-/-$
$s = 1$	Kagome (degenerate)	$+/+/+$ or $-/-/-$
$s = 2$	Square	$+/+$ and $-/-$
$s = 3$	Hexagonal	$+/+/+$ and $-/-/-$

At $d \approx d_{\text{st}}$, the interaction energies associated with the square, hexagonal, and kagome lattices in Fig. 3a lie within 1 $k_B T$ of each other, suggesting an effective degeneracy in the preferred lattice architecture of crown-shaped proteins with $s = 1$. The competition between square, hexagonal, and kagome lattices depends on the specific values of the model parameters considered. The relative energies of these lattice architectures also depend on boundary effects arising from the finite size of the membrane protein lattices considered in Fig. 3a. However, we find that the differences in G_{int} between square, hexagonal, and kagome lattices remain within 1 $k_B T$ of each other as the number of crown-shaped proteins in the lattice, n, is increased (Fig. 3a, leftmost inset). To explore the limit $n \to \infty$, it is instructive to fit G_{int} to its expected asymptotic dependence on n,

$$G_{\text{int}}(n) = G^{\infty} + \frac{1}{\sqrt{n}} G', \qquad (3)$$

where G^{∞} is the interaction energy per protein in infinite lattices and G' captures finite size effects. Taking n to be even, we find in the leftmost inset of Fig. 3a that $(G^{\infty}, G') \approx (-21.1, 20.5)\ k_B T$, $(-21.7, 30.8)\ k_B T$, and $(-21.5, 23.4)\ k_B T$ for square, hexagonal, and kagome lattices, respectively. Odd n yield different boundary effects and, hence, different values of G' in eqn (3) but, within the numerical accuracy used here, the same values of G^{∞} as even n. Figure 3a therefore suggests that, in the limit $n \to \infty$, the hexagonal lattice provides the most favorable lattice architecture by only a fraction of 1 $k_B T$ per protein. As a result, we expect that the effective degeneracy of square, hexagonal, and kagome lattices as the energetically most stable (ground) state of the system in Fig. 3a persists even in the limit of large n. This degeneracy is expected to make the lattice architectures in Fig. 3a susceptible to thermal perturbations, which we discuss further in Sec. 5.

Some of the lattices of crown-shaped proteins with $s = 1$ in Fig. 3a exhibit intriguing patterns in the protein orientation. In particular, we find that the energetically most favorable square, hexagonal, and kagome lattices show, in addition to translational ordering, distinctive azimuthal ordering of neighboring proteins (see Table 1). In contrast, the directional interactions between crown-shaped proteins with $s = 1$ are frustrated in honeycomb lattices, thus preventing similar azimuthal ordering of neighboring proteins. For the kagome lattice, we find azimuthal ordering according to a $+/+/+$ or a $-/-/-$ pattern, in which three nearest-neighbor proteins are oriented so that the portions of their lipid-protein interfaces with $U_i(\theta) > U_i^0$ or $U_i(\theta) < U_i^0$ in eqn (2) point

towards each other. Such $+/+/+$ or $-/-/-$ triplets of crown-shaped proteins with $s = 1$ provide a shared locus for large lipid bilayer thickness deformations and, as discussed further in Sec. 5, are therefore highly favorable from an energetic perspective. For the hexagonal lattice, similar triplet motifs are favored, but with each crown-shaped protein being part of a $+/+/+$ triplet *and* a $-/-/-$ triplet. This interaction pattern results in alternating "bands" of membrane regions in the hexagonal lattice with increased or decreased hydrophobic thickness. In the square lattice, each crown-shaped protein forms one $+/+$ and one $-/-$ interaction pair with its nearest neighbors. This can be understood by noting that, as shown in Fig. 2, such $+/+$ and $-/-$ configurations are minima of the pair interaction energy. In the square lattice we thus obtain, similarly as in the hexagonal lattice, bands of membrane regions with increased or decreased hydrophobic thickness.

For crown-shaped proteins with $s = 2$ (see Fig. 3b), we find that the honeycomb, square, and kagome lattices yield a qualitatively similar dependence of G_{int} on d as obtained with $s = 1$ in Fig. 3a. In contrast, hexagonal lattices of crown-shaped proteins with $s = 2$ yield, due to frustration in the azimuthal ordering of neighboring proteins, highly unfavorable interactions at small d. As d is increased in hexagonal lattices with $s = 2$, G_{int} decreases and attains a minimum, with $|G_{int}| < 1$ $k_B T$ for $d \gtrsim 11$ nm. In contrast, the bilayer-thickness-mediated protein interactions in honeycomb, square, and kagome lattices become increasingly favorable as d is decreased, with $G_{int} < 0$ for $d \lesssim 8$ nm. In particular, the square lattice allows each protein to interact with all its nearest neighbors in $+/+$ or $-/-$ configurations (Fig. 3b, inset), and hence provides a particularly favorable arrangement for crown-shaped proteins with $s = 2$. Figure 3b suggests that the square lattice with $d = d_{st}$ yields the ground state lattice architecture for crown-shaped proteins with $s = 2$ (Table 1). The kagome lattice provides the second most favorable lattice architecture in Fig. 3b, for which, similarly as in Fig. 3a, $-/-/-$ triplets yield an energetically favorable nearest-neighbor interaction motif (Fig. 3b, inset).

Finally, we consider crown-shaped proteins with $s = 3$ (see Fig. 3c). We find that the hexagonal lattice provides the energetically most favorable arrangement of crown-shaped proteins with $s = 3$ for a wide range of d, as well as the ground state lattice architecture at $d = d_{st}$ (Table 1). The stability of the hexagonal lattice architecture for $s = 3$ arises from the compatibility between the six-fold symmetry of the hexagonal lattice and the three-fold protein symmetry of crown-shaped proteins with $s = 3$, which allows each protein to interact with all its nearest neighbors in highly favorable $+/+/+$ or $-/-/-$ triplet configurations (Fig. 3c, inset). We also note that the kagome lattice in Fig. 3c, in which each protein is part of a $+/+/+$ as well as a $-/-/-$ triplet, yields similar interaction energies as the square lattice. The square lattice has a higher protein packing density than the kagome lattice, but does not permit similarly favorable azimuthal ordering of neighboring proteins. The comparable energies associated with the kagome and square lattices in Fig. 3c thus illustrate the competition between translational and azimuthal ordering in setting the energetically favorable lattice architectures of crown-shaped proteins.

5 Membrane protein meshes

While bilayer-thickness-mediated interactions between crown-shaped proteins favor the lattice architectures shown in Fig. 3 and Table 1, thermal fluctuations are generally expected to perturb, or even disrupt, these lattice architectures. In particular, the effective degeneracy in the ground state lattice architecture of crown-shaped proteins with $s = 1$, and the relative weakness of the lattice interaction energies for $s = 1$ compared to $s = 2$ and $s = 3$ in Fig. 3, suggest that lattices of crown-shaped proteins with $s = 1$ are particularly susceptible to thermal perturbations. In this section, we explore, based on crown-shaped proteins with $s = 1$, the effect of thermal perturbations on the large-scale organization of membrane proteins with anisotropic hydrophobic thickness.

The effective degeneracy in the ground state lattice architecture for $s = 1$ in Fig. 3a suggests that various local interaction motifs, such as different protein pair and triplet configurations, yield comparable interaction energies for crown-shaped proteins with $s = 1$. Figure 4 illustrates that, even for small protein numbers, there indeed exist several distinct, and energetically favorable, protein configurations with interaction energies within just a few $k_B T$ of each other. The basic building blocks for these favorable protein configurations are the $+/+$ and $-/-$ pair and $+/+/+$ and $-/-/-$ triplet configurations discussed in Sec. 4. From the perspective of large-scale protein organization, one expects that the $+/+$ and $-/-$ pair interaction motifs favor elongated structures while the triplet interaction motifs may give rise to branched structures. In the presence of thermal fluctuations, pairs and triplets of crown-shaped proteins may thus produce large-scale, mesh-like structures reminiscent of cross-linked polymer networks[70].

To further investigate the effect of thermal fluctuations on the supramolecular organization of crown-shaped proteins with $s = 1$, we performed finite temperature Monte Carlo simulations (see Fig. 5). Even with the efficient FE approach for the minimization of eqn (1) used here, finite temperature Monte Carlo simulations of hundreds of interacting crown-shaped proteins present formidable computational challenges. To render the computations more tractable, we made two simplifying assumptions in Fig. 5. First, we did not consider the full multi-body interactions between crown-shaped proteins but, instead, employed the pair interaction potentials implied by eqn (1), which we calculated using FEs[47,49,55]. Second, we did not allow in Fig. 5 for the collective dynamics[71,72] of crown-shaped proteins or effects arising from the hydrodynamics of the lipid bilayer[73,74]. Due to the simplifying assumptions summarized above, we only expect the FE computations and Monte Carlo simulations used for Fig. 5 to capture broad features of the finite temperature organization of crown-shaped proteins with $s = 1$, and not the precise numerical values of the bilayer-thickness-mediated protein interaction energies or the dynamics of protein diffusion.

The Monte Carlo simulations in Fig. 5 were performed at room temperature starting from random initial conditions. Figure 5 suggests that crown-shaped proteins with $s = 1$ can self-assemble into mesh-like structures. For a given average areal density of crown-shaped proteins, ϕ, we quantified the structure of the pro-
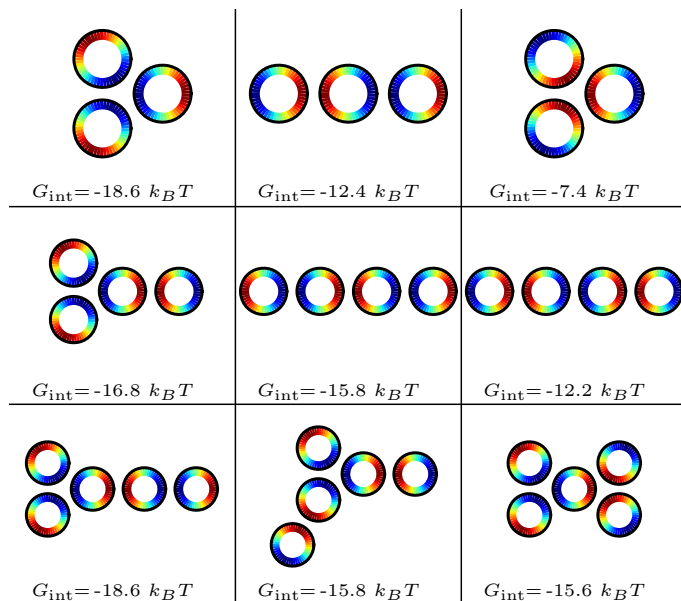
Fig. 4 Examples of energetically favorable configurations of crown-shaped proteins with $s = 1$ for the protein numbers $n = 3$ (first row), $n = 4$ (second row), and $n = 5$ (third row) together with the corresponding interaction energy per protein due to bilayer-thickness-mediated protein interactions, G_{int}. We obtained G_{int} from the full multi-body interaction energies via minimization of eqn (1) using FEs[47,49,55]. In each protein configuration, the nearest-neighbor protein separation is given by $d = d_{\text{st}}$. The coloring of crown-shaped proteins follows the u-scale in Fig. 1.

Fig. 5 Average mesh area $\langle A_{\text{poly}} \rangle$ in mesh-like, finite temperature structures formed by crown-shaped proteins with $s = 1$, scaled by the effective protein area A_{p}, versus average protein areal density ϕ. In our simulations we employed a square-shaped simulation box of edge length $L = 100$ nm with periodic boundary conditions. We therefore have $\phi = nA_{\text{p}}/L^2$, where n is the protein number. All results were obtained through room temperature Monte Carlo simulations with pair interaction potentials (see Appendix A) and $d \geqslant d_{\text{st}}$. For each value of ϕ reported, we performed 30 Monte Carlo simulations with different, randomly-generated initial conditions. In each simulation we carried out 10^7 Monte Carlo steps, and sampled the protein configuration every 10^6 steps. The error bars indicate the standard errors about $\langle A_{\text{poly}} \rangle$. The insets show snapshots of the simulation domain at various ϕ. The crown-shaped proteins with effective area A_{p} are indicated in black. Membrane compartments are colored for ease of visualization. When computing $\langle A_{\text{poly}} \rangle$ we did not consider contributions due to very small loops formed by six or fewer proteins.

tein meshes through the average mesh area, $\langle A_{\text{poly}} \rangle$. To calculate $\langle A_{\text{poly}} \rangle$ we connected the centers of nearest-neighbor crown-shaped proteins by straight lines yielding, for protein chains that close up over the scale of the simulation domain, finite polygonal loops. For each polygonal loop we calculated the loop area, from which we computed the associated "free" area of the polygonal loop available to proteins inside the loop, A_{poly}, by subtracting the portion of the loop area effectively occupied by the proteins forming the boundary of the polygonal loop (Fig. 5, insets). For the latter calculation, we modeled the effective cross section of crown-shaped proteins in the plane of the membrane by a disk of area $A_{\text{p}} = \pi R^2$, where $R = R_i + R_l$ with $R_l = 0.5$ nm to take into account steric constraints arising from the finite size of lipids. We obtained $\langle A_{\text{poly}} \rangle$ by averaging A_{poly} over the simulation domain, multiple Monte Carlo steps, and Monte Carlo runs with distinct (random) initial conditions (see Fig. 5 and Appendix A).

Depending on the areal density of crown-shaped proteins, the average mesh area $\langle A_{\text{poly}} \rangle$ associated with the protein meshes in Fig. 5 can exceed the effective protein area A_{p} by more than one order of magnitude, thus yielding sizable membrane compartments. The finite temperature, mesh-like organization of crown-shaped proteins in Fig. 5 should be contrasted with the compact ground state lattice architectures in Fig. 3a produced by bilayer-thickness-mediated protein interactions in the absence of thermal fluctuations. The protein meshes found in our Monte Carlo simulations are only transiently stable. Characterization of the dynamics of protein meshes will require more detailed modeling of the diffusion dynamics of crown-shaped proteins in mem-

branes[71–74]. Figure 5 suggests a non-monotonic dependence of $\langle A_{\text{poly}} \rangle$ on ϕ with $\langle A_{\text{poly}} \rangle$ being maximal for some ϕ. Such a non-monotonic dependence of $\langle A_{\text{poly}} \rangle$ on ϕ can be understood intuitively by noting that, at small ϕ, the protein meshes are not large enough to span the entire system, with (infinitely) large protein-free domains percolating through the system and a few small closed loops of crown-shaped proteins (see the leftmost inset in Fig. 5). As ϕ is increased, the protein meshes span a larger and larger fraction of the system, and $\langle A_{\text{poly}} \rangle$ increases. But, for large enough ϕ, the mesh structure is disrupted by the high protein density, resulting in a decrease in the average mesh area.

6   Conclusions

Bilayer-mediated interactions between membrane proteins provide a general physical mechanism for the self-assembly of membrane protein lattices. One particularly favorable mode of bilayer-mediated protein interactions is provided by bilayer-thickness-mediated protein interactions arising from a hydrophobic thickness mismatch between membrane proteins and the unperturbed lipid bilayer[27,28,32,34–36,45,47,49,52,60]. Since different membrane proteins, or even different conformational states of the same membrane protein, often show distinct hydrophobic thicknesses, protein-induced lipid bilayer thickness deformations are a ubiquitous feature of bilayer-protein interactions[15–20,23–25,39,63]. For membrane proteins with a non-circular cross section or anisotropic hydrophobic thickness, bilayer-thickness-mediated protein interactions not only depend on the protein separation but also on the protein orientation[45,47,49,52,55]. Based on a sim-

ple model of anisotropic protein hydrophobic thickness, we have established here general relations between the azimuthal symmetry of bilayer-protein interactions and the supramolecular organization of membrane proteins.

Our results show that the symmetry of the protein hydrophobic thickness is reflected in the directionality of bilayer-thickness-mediated protein interactions, with the energy landscape of bilayer-thickness-mediated protein interactions depending crucially on protein symmetry. Carrying out multi-body calculations of bilayer-thickness-mediated protein interactions in systems composed of hundreds of membrane proteins, we find that distinctive protein symmetries yield distinctive ground state lattice architectures of membrane protein clusters. In particular, for membrane proteins with one-fold rotational symmetry [$s = 1$ in eqn (2)] our results suggest an effective degeneracy in the ground state lattice architecture, with square, hexagonal, and kagome lattices being approximately equally favorable. In contrast, membrane protein dimers with two-fold rotational symmetry [$s = 2$ in eqn (2)] imply a ground state lattice architecture with square symmetry, while membrane protein trimers with three-fold rotational symmetry [$s = 3$ in eqn (2)] yield a hexagonal ground state lattice architecture. Distinctive membrane protein lattice architectures are expected to produce distinctive collective responses of membrane protein lattices[8,9,18,55], and can thus affect the biological function of membrane proteins in cell membranes.

In general, the translational and rotational ordering of membrane proteins found here may be perturbed, or even disrupted, by thermal fluctuations, heterogeneities in cell membrane composition, or protein interactions other than the bilayer-thickness-mediated protein interactions considered here, such as direct protein-protein interactions and bilayer-curvature-mediated protein interactions. The effective degeneracy in the ground state lattice architecture found for $s = 1$ makes the supramolecular organization of membrane proteins with $s = 1$ particularly susceptible to such perturbations. Indeed, our results suggest that thermal fluctuations transform the ground state lattice architecture of membrane proteins with $s = 1$ into transiently stable, mesh-like structures. These protein meshes divide the membrane into compartments with in-plane areas that can be more than one order of magnitude greater than the cross-sectional area of individual proteins in the plane of the membrane. Bilayer-thickness-mediated protein interactions thus provide a mechanism for membrane compartmentalization at scales of tens of nanometers, which may allow the transient trapping of membrane proteins and lipids in specific membrane regions. Supramolecular organization of cell membranes into membrane compartments is thought to be crucial for many essential biological functions of cell membranes[1,58,59,75,76]. Unlike other potential mechanisms for membrane organization[58,59], the protein meshes found here emerge directly from bilayer-mediated protein interactions and, in particular, do not rely on interactions with structures outside the cell membrane such as the cytoskeleton.

The bilayer-thickness-mediated protein interactions considered here are reminiscent of capillary interactions between micron- and submicron-sized particles at fluid-fluid interfaces[77]. Similarly as capillary interactions, bilayer-thickness-mediated protein

interactions can be studied analytically using multipole expansions[45]. Indeed, multipole expansions allow exact analytic solutions for the bilayer-thickness-mediated interactions between two crown-shaped proteins, which are in excellent agreement with the corresponding numerical solutions obtained from the FE approach used here[49]. However, capillary and bilayer-thickness-mediated interactions have different physical origins, with the latter being short-ranged[55]. Finally we note that, based on recent advances in computational protein design[78,79], it is becoming increasingly feasible to design membrane proteins with specific properties, such as the periodic variations in protein hydrophobic thickness considered here. The results described here may help in the design of membrane proteins that self-assemble in membrane environments into supramolecular structures with predefined properties. The approach developed here may thus provide insights into large-scale membrane protein organization not only in naturally occurring but also artificial membrane systems[80].

Acknowledgments

Appendix

A Monte Carlo simulations

To fix the protein orientations in Fig. 3, and to explore in Fig. 5 the effect of thermal fluctuations on the supramolecular organization of crown-shaped proteins with $s = 1$, we carried out Metropolis Monte Carlo simulations[81] with pair interaction potentials. For the results presented in Fig. 5, we performed our Monte Carlo simulations at room temperature $T_{rm} = 298$ K. For Fig. 3, we searched for low-energy protein orientations using a simulated annealing Monte Carlo approach with linear cooling[82], decreasing the (effective) temperature in the Monte Carlo simulations from $T \approx 5 T_{rm}$ to $T = 0$.

For the parameter values used here, the bilayer-thickness-mediated protein interactions effectively vanish for $d \gtrsim 15$ nm. To accelerate pair evaluations in our Monte Carlo simulations we therefore implemented cell list structures[81] using a cutoff $d = 15$ nm on the range of bilayer-thickness-mediated protein interactions. In particular, we constructed a table of bilayer-thickness-mediated interaction energies $G_{int}(d, \omega_1, \omega_2)$ for protein pairs, which we computed using FEs with a translational resolution $\Delta d = 0.25$ nm and a resolution $\Delta \omega = 3°$ in the relative protein orientations. During Monte Carlo runs, we estimated the pair interaction energies for arbitrary values of (d, ω_1, ω_2) by first rounding ω_1 and ω_2 to their closest values in the aforementioned table, and then linearly interpolating $G_{int}(d, \omega_1, \omega_2)$ with respect to d to obtain the interaction energy for the appropriate value of d.

For the results in Fig. 5 we performed, at each Monte Carlo step, on average one displacement and one rotation trial per protein. For Fig. 3, the positions of the proteins were kept fixed according to the lattice structures of interest and we only allowed rotation trials. We used in our Monte Carlo simulations the trans-

lation and rotation increments $\delta d = 0.1$ nm and $\delta \omega = 2°$, respectively. We note that, assuming a unit time step $\delta t = 10^{-9}$ s, these displacement and rotation increments correspond to a translational diffusion coefficient $D_T \approx \delta d^2 / 4 \delta t \approx 2.5\ \mu\text{m}^2/\text{s}$ and a rotational diffusion coefficient $D_R \approx \delta \omega^2 / 2 \delta t \approx 6.1 \times 10^5\ \text{rad}^2/\text{s}$, which are consistent with previous work on the diffusion of membrane proteins in lipid bilayers [21,83].

References

1 D. M. Engelman, *Nature*, 2005, **438**, 578.

2 N. Destainville, T. H. Schmidt and T. Lang, *Curr. Top. Membr.*, 2016, **77**, 27.

3 P. Recouvreux and P.-F. Lenne, *Curr. Opin. Cell Biol.*, 2016, **38**, 18–23.

4 S. Bahatyrova *et al.*, *Nature*, 2004, **430**, 1058–1063.

5 D. Baddeley *et al.*, *Proc. Natl. Acad. Sci. U.S.A.*, 2009, **106**, 22275–22280.

6 A. Briegel *et al.*, *eLife*, 2014, **3**, e02151.

7 B. F. Lillemeier, M. A. Mörtelmaier, M. B. Forstner, J. B. Huppa, J. T. Groves and M. M. Davis, *Nat. Immunol.*, 2010, **11**, 90–96.

8 T. Duke and D. Bray, *Proc. Natl. Acad. Sci. U.S.A.*, 1999, **96**, 10104–10108.

9 V. Sourjik, *Trends in Microbiology*, 2004, **12**, 569 – 576.

10 J.-H. Jeon, M. Javanainen, H. Martinez-Seara, R. Metzler and I. Vattulainen, *Phys. Rev. X*, 2016, **6**, 021006.

11 R. Metzler, J.-H. Jeon and A. Cherstvy, *BBA-Biomembranes*, 2016, **1858**, 2451–2467.

12 S.-Y. Park *et al.*, *Nat. Struct. Mol. Biol.*, 2006, **13**, 400–407.

13 J. J. Sieber *et al.*, *Science*, 2007, **317**, 1072–1076.

14 A. Briegel *et al.*, *Biochemistry*, 2014, **53**, 1575–1585.

15 T. A. Harroun *et al.*, *Biophys. J.*, 1999, **76**, 937.

16 R. L. Goforth *et al.*, *J. Gen. Physiol.*, 2003, **121**, 477–493.

17 A. V. Botelho *et al.*, *Biophys. J.*, 2006, **91**, 4464 – 4477.

18 S. L. Grage *et al.*, *Biophys. J.*, 2011, **100**, 1252 – 1260.

19 D. Milovanovic *et al.*, *Nat. Commun.*, 2015, **6**, 5984.

20 A. M. Pollard and V. Sourjik, *J. Biol. Chem.*, 2018, **293**, 2149–2158.

21 X. Periole, T. Huber, S.-J. Marrink, and T. P. Sakmar, *J. Am. Chem. Soc.*, 2007, **129**, 10126–10132.

22 D. Parton, J. Klingelhoefer and M. Sansom, *Biophys. J.*, 2011, **101**, 691 – 699.

23 H.-J. Kaiser *et al.*, *Proc. Natl. Acad. Sci. U.S.A.*, 2011, **108**, 16628–16633.

24 S. Mondal, J. M. Johnston, H. Wang, G. Khelashvili, M. Filizola and H. Weinstein, *Sci. Rep.*, 2013, **3**, 2909.

25 S. Mondal, G. Khelashvili and H. Weinstein, *Biophys. J.*, 2014, **106**, 2305.

26 M. Goulian, R. Bruinsma and P. Pincus, *EPL*, 1993, **22**, 145.

27 N. Dan, P. Pincus and S. A. Safran, *Langmuir*, 1993, **9**, 2768–2771.

28 H. Aranda-Espinoza, A. Berman, N. Dan, P. Pincus and S. Safran, *Biophys. J.*, 1996, **71**, 648 – 656.

29 R. Golestanian, M. Goulian and M. Kardar, *Phys. Rev. E*, 1996, **54**, 6725.

30 T. R. Weikl, M. M. Kozlov and W. Helfrich, *Phys. Rev. E*, 1998, **57**, 6988.

31 K. S. Kim, J. Neu and G. Oster, *Biophys. J.*, 1998, **75**, 2274–2291.

32 J.-B. Fournier, *Eur. Phys. J. B.*, 1999, **11**, 261–272.

33 T. Weikl, *EPL*, 2001, **54**, 547.

34 M. B. Partenskii, G. V. Miloshevsky and P. C. Jordan, *J. Chem. Phys.*, 2004, **120**, 7183–7193.

35 G. Brannigan and F. L. H. Brown, *Biophys. J.*, 2007, **92**, 864–876.

36 T. Ursell, K. C. Huang, E. Peterson and R. Phillips, *PLoS Comput. Biol.*, 2007, **3**, e81.

37 K. S. Kim, T. Chou and J. Rudnick, *Phys. Rev. E*, 2008, **78**, 011401.

38 R. N. Frese *et al.*, *Biophys. J.*, 2008, **94**, 640–647.

39 R. Phillips, T. Ursell, P. Wiggins and P. Sens, *Nature*, 2009, **459**, 379.

40 T. Auth and G. Gompper, *Phys. Rev. E*, 2009, **80**, 031901.

41 M. M. Müller and M. Deserno, *Progr. Theor. Phys. Suppl.*, 2010, **184**, 351–363.

42 H.-K. Lin, R. Zandi, U. Mohideen and L. P. Pryadko, *Phys. Rev. Lett.*, 2011, **107**, 228104.

43 B. J. Reynwar and M. Deserno, *Soft Matter*, 2011, **7**, 8567–8575.

44 P. Dommersnes and J.-B. Fournier, *Eur. Phys. J. B*, 1999, **12**, 9–12.

45 C. A. Haselwandter and R. Phillips, *EPL*, 2013, **101**, 68002.

46 S. Weitz and N. Destainville, *Soft Matter*, 2013, **9**, 7804–7816.

47 O. Kahraman, W. S. Klug and C. A. Haselwandter, *EPL*, 2014, **107**, 48004.

48 C. Yolcu, R. C. Haussman and M. Deserno, *Adv. Colloid Interface Sci.*, 2014, **208**, 89–109.

49 O. Kahraman, P. D. Koch, W. S. Klug and C. A. Haselwandter, *Phys. Rev. E*, 2016, **93**, 042410.

50 T. R. Weikl, *Ann. Rev. Phys. Chem.*, 2018, **69**, 521–539.

51 C. A. Haselwandter and R. Phillips, *PLoS Comput. Biol.*, 2013, **9**, e1003055.

52 C. A. Haselwandter and N. S. Wingreen, *PLoS Comput. Biol.*, 2014, **10**, e1003932.

53 Y. Schweitzer and M. M. Kozlov, *PLoS Comput. Biol.*, 2015, **11**, e1004054.

54 H. Noguchi and J.-B. Fournier, *Soft Matter*, 2017, **13**, 4099–4111.

55 O. Kahraman, P. D. Koch, W. S. Klug and C. A. Haselwandter, *Sci. Rep.*, 2016, **6**, 19214.

56 M. Lindén, P. Sens and R. Phillips, *PLoS Comput. Biol.*, 2012, **8**, e1002431.

57 L. R. Forrest, *Ann. Rev. Biophys.*, 2015, **44**, 311–337.

58 A. Kusumi, Y. M. Shirai, I. Koyama-Honda, K. G. Suzuki and T. K. Fujiwara, *FEBS Lett.*, 2010, **584**, 1814–1823.

59 A. Kusumi, T. A. Tsunoyama, K. M. Hirosawa, R. S. Kasai and

T. K. Fujiwara, *Nat. Chem. Biol.*, 2014, **10**, 524–532.

60 T. A. Harroun *et al.*, *Biophys. J.*, 1999, **76**, 3176.

61 A. R. Evans, M. S. Turner and P. Sens, *Phys. Rev. E*, 2003, **67**, 041907.

62 H. W. Huang, *Biophys. J.*, 1986, **50**, 1061–1070.

63 O. S. Andersen and R. E. Koeppe, II, *Annu. Rev. Biophys. Biomol. Struct.*, 2007, **36**, 107–120.

64 T. Ursell, J. Kondev, D. Reeves, P. A. Wiggins and R. Phillips, Mechanosensitivity in Cells and Tissues 1: Mechanosensitive Ion Channels, New York, 2008, pp. 37–70.

65 W. Rawicz *et al.*, *Biophys. J.*, 2000, **79**, 328–339.

66 K. Mitra, I. Ubarretxena-Belandia, T. Taguchi, G. Warren and D. M. Engelman, *Proc. Natl. Acad. Sci. U.S.A.*, 2004, **101**, 4083.

67 G. Chang, R. H. Spencer, A. T. Lee, M. T. Barclay and D. C. Rees, *Science*, 1998, **282**, 2220–2226.

68 P. Wiggins and R. Phillips, *Proc. Natl. Acad. Sci. U.S.A.*, 2004, **101**, 4071.

69 N. Dan, A. Berman, P. Pincus and S. A. Safran, *J. Phys. II*, 1994, **4**, 1713–1725.

70 C. P. Broedersz and F. C. MacKintosh, *Rev. Mod. Phys.*, 2014, **86**, 995–1036.

71 E. Luijten and J. Liu, *AIP Conference Proceedings*, 2003, **690**, 225–231.

72 S. Whitelam, E. H. Feng, M. F. Hagan and P. L. Geissler, *Soft Matter*, 2009, **5**, 1251–1262.

73 B. A. Camley and F. L. H. Brown, *Soft Matter*, 2013, **9**, 4767–4779.

74 E. Noruzifar, B. A. Camley and F. L. H. Brown, *J. Chem. Phys.*, 2014, **141**, 124711.

75 A. Mugler, F. Tostevin and P. R. ten Wolde, *Proc. Natl. Acad. Sci. U.S.A.*, 2013, **110**, 5927–5932.

76 P. D. Calvert, V. I. Govardovskii, N. Krasnoperova, R. E. Anderson, J. Lem and C. L. Makino, *Nature*, 2001, **411**, 90–94.

77 L. Botto, E. P. Lewandowski, M. Cavallaro and K. J. Stebe, *Soft Matter*, 2012, **8**, 9957–9971.

78 J. M. Perez-Aguilar and J. G. Saven, *Structure*, 2012, **20**, 5–14.

79 R. F. Alford *et al.*, *PLoS Comput. Biol.*, 2015, **11**, 1–23.

80 P. V. Escribá *et al.*, *Progress in Lipid Research*, 2015, **59**, 38 – 53.

81 D. Frenkel and B. Smit, *Understanding Molecular Simulation*, Academic Press, 2nd edn, 2001.

82 W. H. Press, S. A. Teukolsky, W. T. Vetterling and B. P. Flannery, *Numerical Recipes*, Cambridge University Press, 3rd edn, 2007.

83 R. Peters and R. J. Cherry, *Proc. Natl. Acad. Sci. U.S.A.*, 1982, **79**, 4317–4321.

Text for graphical abstract:

Azimuthal variations in membrane protein hydrophobic thickness can yield self-assembly of distinctive protein lattices and produce membrane compartmentalization.